Journal of
Composites Science

MDPI

Article

Photocatalytic Decomposition of Rhodamine B and Selective Oxidation of 5-Hydroxymethylfurfural by β-Bi_2O_3/$Bi_{12}SiO_{20}$ Nanocomposites Produced by Laser

Aleksandra G. Golubovskaya [1], Tamara S. Kharlamova [2], Ekaterina A. Gavrilenko [1], Elena D. Fakhrutdinova [1], Olga V. Vodyankina [2], Sergei A. Kulinich [3,*] and Valery A. Svetlichnyi [1,*]

[1] Laboratory of Advanced Materials and Technology, Tomsk State University, Tomsk 634050, Russia
[2] Laboratory of Catalytic Research, Chemistry Department, Tomsk State University, Tomsk 634050, Russia
[3] Research Institute of Science and Technology, Tokai University, Hiratsuka 259-1292, Kanagawa, Japan
* Correspondence: skulinich@tokai-u.jp (S.A.K.); v_svetlichnyi@bk.ru (V.A.S.)

Abstract: In this work, we studied the catalytic performance of a β-Bi_2O_3/$Bi_{12}SiO_{20}$ nanocomposite material in the reactions involving the photodecomposition of rhodamine B and selective photooxidation of 5-hydroxymethylfurfural (HMF). The semiconductor composite nanomaterial was obtained by means of the mechanical grinding of a mixture of nanopowders of β-Bi_2O_3 and sillenite, both individually produced via pulsed laser ablation. The crystal structure of the prepared composite particles was confirmed by means of X-ray diffraction, while the optical properties of both individual components and their composite (with different ratios of Bi_2O_3 and $Bi_{12}SiO_{20}$) were also studied. The photocatalytic activity of the composite particles was studied in the course of their decomposition of rhodamine B under LED excitation at wavelengths of 375, 410 and 470 nm. It was shown that the optimal β-Bi_2O_3/$Bi_{12}SiO_{20}$ ratio in the composite particles resulted in their photocatalytic activity exceeding those of both single-phase β-Bi_2O_3 and $Bi_{12}SiO_{20}$, as well as that of their mixtures (by ~2.3 times for the excitation of an LED with λ = 375 nm). The novel composite particles were also found to perform better in the selective photocatalytic oxidation of HMF: at a conversion of ~5%, the selectivity toward DFF of the nanocomposite was significantly higher (10.3%) than that of sample Bi_2O_3 (−4.2%). A model was proposed that explains the increase in activity of the newly prepared photocatalyst due to the formation of a type II heterojunction in its particles.

Keywords: pulsed laser ablation; β-Bi_2O_3; sillenite; semiconductor nanocomposites; photocatalysis; rhodamine B; 5-hydroxymethylfurfural; type II heterojunction

Citation: Golubovskaya, A.G.; Kharlamova, T.S.; Gavrilenko, E.A.; Fakhrutdinova, E.D.; Vodyankina, O.V.; Kulinich, S.A.; Svetlichnyi, V.A. Photocatalytic Decomposition of Rhodamine B and Selective Oxidation of 5-Hydroxymethylfurfural by β-Bi_2O_3/$Bi_{12}SiO_{20}$ Nanocomposites Produced by Laser. *J. Compos. Sci.* **2024**, *8*, 42. https://doi.org/10.3390/jcs8020042

Academic Editor: Aleksey A. Vedyagin

Received: 17 November 2023
Revised: 28 December 2023
Accepted: 22 January 2024
Published: 24 January 2024

1. Introduction

Recently, there has been a growing demand for "green" photocatalytic technologies that aim at solving environmental problems. One such problem is water pollution with organic compounds (e.g., phenol derivatives, herbicides, dyes, antibiotics and other molecules) that enter the water from various man-made sources, including textile, pulp and paper and pharmaceutical plants and factories [1–3]. Another promising area in photocatalysis is the processing of renewable resources, such as biomass, in particular the transformation of 5-hydroxymethylfurfural (HMF) extracted from lignocellulosic biomass (which is the most accessible raw material on Earth), into valuable products with high added value [4]. Research in this area has been extensively developing over the past few years [5–7], also aiming at the simultaneous production of hydrogen [8].

The development of effective and stable photocatalysts for water purification from organic pollutants and for selective transformations in biomass processing, which are also non-toxic and capable of operating in both the UV and visible spectral ranges, remains an important aspect for the advancement of this technology. Such materials include, for example, classical oxide photocatalysts based on wide-gap titanium (TiO_2) and zinc

(ZnO) oxides as part of heterostructures [9,10], or composite and decorated materials with plasmonic particles [11,12], as well as a large number of other semiconductor photocatalysts, including carbon-based materials [13].

A conventional semiconductor particle has a number of disadvantages related to the insufficient separation and rapid recombination of charge carriers, as well as to its limited spectral range [14,15]. An effective way to overcome them and improve the photocatalytic properties of the material is to create heterostructures [16–18]. Several types of heterostructures can be distinguished, depending on their bandgap width, energy band positions, the relationship between the semiconductors forming the heterostructure, as well as the migration and relaxation paths of the electron–hole pairs [19]. Based on modern ideas about photocatalytic mechanisms, it is the type II heterostructures and z-scheme that can be effective [15,20,21]. In turn, the z-scheme can be of three types: conventional z-scheme heterojunction, all-solid-state z-scheme, and direct z-scheme heterojunction [22]. Different types of dual z-scheme heterojunctions can be considered when three semiconductors are involved [17]. In recent years, the so-called s-scheme [23,24] has also been proposed, which can be considered an improved version of the z-scheme [24].

Among a wide range of oxide catalysts, not the least place is occupied by various bismuth-based nanomaterials [25]. Good photocatalytic properties are exhibited by both various polymorphic modifications of bismuth oxide Bi_2O_3 and more complex compounds, for example, double oxides such as silicates (BSO), titanates (BTO), tungstates (BWO), vanadates (BVO), etc. Because of their remarkable physical and chemical properties, ability to adjust their band gap, good biocompatibility and chemical stability, various modifications of bismuth silicates are widely studied [26].

The metastable phase of bismuth oxide β-Bi_2O_3 is known to absorb radiation up to 500 nm (band gap E_g~2.4 eV), and it demonstrates good photocatalytic activity when excited by visible light [27]; however, the rapid recombination of charge carriers reduces the efficiency of such materials [28]. This problem, as mentioned above, can be solved by implementing a type II heterojunction, which is expected to lead to effective charge separation and, thus, permits the creation of nanocomposite (NC) particles with enhanced photocatalytic activity [15]. Unlike its stable α counterpart, the β phase of bismuth oxide has ionic conductivity. The latter conductivity is believed to be provided by oxygen ions, which easily move inside the particle [29]. Typically, β-Bi_2O_3 is referred to as an indirect-gap *p*-type semiconductor [30], although there are works where it shows *n*-conductivity [28]. This oxide was reported to form heterojunctions with wider-gap *n*-type semiconductors, for example, TiO_2 [31] and ZnO [32], as well as with the bismuth-containing compounds BVO, BMO, BiOI, and so on [10,28].

A suitable candidate for creating a type II heterojunction with β-Bi_2O_3 may be sillenite $Bi_{12}SiO_{20}$, which also exhibits photocatalytic properties [33]. Sillenite is a semiconductor with a unique structure of energy levels that exhibits photorefractive properties and has a direct-gap energy structure [34,35], with a band gap of about 3.2 eV [36]. In dark conditions, this semiconductor has *p*-type conductivity [35]. It was shown experimentally and theoretically that due to the large number of trap sites in its band gap, which are filled during photoexcitation, sillenite experiences a shift in the Fermi level and shows *n*-type conductivity [37]. Thus, at a distance of about 2.2 eV below the conduction band (CB), $Bi_{12}SiO_{20}$ was shown to have an electron donor center ($Bi_{Si}^{3+} + h^+$) [36]. This level belongs to the valence band (VB) and is partially occupied, which leads to the photorefractive effect and incorrect determination of E_g [33,38].

Among the wide range of preparation methods for photocatalysts based on bismuth oxides and silicates [25,26,38], recently, laser processing approaches were used [39–42]. It should be noted that due to their variability, environmental friendliness and a number of other advantages [43], methods based on laser ablation became widely used for the production of catalysts [44,45]. This way, using various approaches, including laser ablation in liquid and air, as well as laser processing of complex colloids, we recently obtained a variety of bismuth-based structures, including single-phase samples [41,46–48].

In the present work, we developed a new and simple technique for obtaining β-Bi_2O_3/$Bi_{12}SiO_{20}$ NC particles using "pure" nanoparticles obtained via a laser. The aim of this new approach, combining different types of laser ablation and mechanical grinding, was to obtain a heterostructure that permits us to increase the catalytic activity of its individual components. We then studied their structural and optical properties, and finally tested the photocatalytic activity of the resulting materials during the photodecomposition of the persistent model dye rhodamine B and selective photooxidation of 5-hydroxymethylfurfural.

2. Materials and Methods

2.1. Material Preparation

Particles of β-Bi_2O_3/$Bi_{12}SiO_{20}$ NC were prepared using the following procedure. At the beginning, "pure" particles of β-Bi_2O_3 and $Bi_{12}SiO_{20}$ were produced separately. For this, various variants of laser synthesis were used. For the material preparation, focused Nd:YAG laser radiation (1064 nm, 20 Hz, 7 ns, and 150 mJ) was used in all cases. NPs of β-Bi_2O_3 were directly obtained via pulsed laser ablation (PLA) of the bulk target of metallic bismuth (99.5% purity) in air under ambient conditions. More details of the experimental setup used can be found elsewhere [49]. The resulting nanoparticles were similar to those previously reported by us elsewhere [47]. To reduce the content of unoxidized metallic bismuth and reduce the particle sizes, the process was carried out at a higher irradiation power density on the target (~1 GW/cm^2) than in the earlier work [47]. Hereafter, this sample is denoted as Bi_2O_3.

The preparation of $Bi_{12}SiO_{20}$ (sillenite) nanoparticles was carried out according to the method developed for the preparation of single-phase bismuth metasilicate Bi_2SiO_5 [46], which combines laser ablation, plasma laser treatment of the colloidal mixture, drying and powder annealing. At the first stage, the bulk targets of Bi (99.5%) and Si (99.9%) were ablated in distilled water, resulting in individual colloids, which were then mixed at a molar Bi:Si ratio of 12:1. The mixed colloidal solution was then irradiated with a focused laser beam for 2 h. Such exposure stimulated interactions between the particles, leading to the formation of Bi–Si interfaces, as was previously shown in ref. [41]. The as-prepared (irradiated) colloid was dried in air at 60 °C, after which the resulting powder was annealed at 600 °C in a muffle furnace to form a single-phase bismuth silicate with a sillenite structure $Bi_{12}SiO_{20}$ (the sample denoted as BSO below).

Nanocomposite particles were obtained by grinding a mixture of freshly prepared "pure" particles of β-Bi_2O_3 and sillenite ($Bi_{12}SiO_{20}$) with different ratios of components in an agate mortar for 15 min. As a result, a series of β-Bi_2O_3/$Bi_{12}SiO_{20}$ composite powders were obtained (10-Bi_2O_3/90-BSO, 50-Bi_2O_3/50-BSO and 90-Bi_2O_3/10-BSO), where the numbers indicate the mass content of the components in a corresponding composite. To ensure reproducibility, the composite powders were prepared three times. The results of the UV-Vis spectra measurements and the catalytic activity of identical samples prepared in different batches were found to differ by less than 10%.

2.2. Material Characterization Methods

The size and shape of the nanoparticles were analyzed using transmission electron microscopy (TEM), with a CM12 tool from Philips (Eindhoven, The Netherlands). Additionally, the specific surface area was determined via low-temperature nitrogen adsorption using a TriStar II 3020 analyzer (Micromeritics, Norcross, GA, USA). The crystal structure of samples was studied by means of X-ray diffraction (XRD) using an XRD 7000 diffractometer (Shimadzu, Kyoto, Japan). Identification of the phase composition was carried out using the Powder Diffraction Database PDF-4 (ICDD, Newtown Square, PA, USA). The FTIR spectra were obtained using a Tensor 27 spectrometer (Bruker, Rheinstetten, Germany) equipped with a universal ATR MIRacle module (PIKE, Mount Airy, NC, USA) with a crystal plate Diamond/KRS-5. The Raman spectra were recorded under laser excitation at a wavelength of 785 nm using an inVia Raman spectrometer (Renishaw, Gloucester, UK)

with a DM 2500M microscope (Leica, Berlin, Germany) with a 50× objective. The optical properties of the materials were studied using diffuse reflectance spectroscopy (DRS) in the UV-Vis range on a Cary 100SCAN spectrophotometer (Varian, Australia) equipped with a DRA-CA-30I module (Labsphere, North Sutton, NH, USA). The band gaps were estimated by means of the Tauc method using the following Equation (1):

$$(\alpha h\nu)^{1/n} = A(h\nu - E_g), \quad (1)$$

where α is the absorption coefficient, $h\nu$ is the photon energy, A is a constant independent of the energy, E_g is the band gap energy, and parameter $n = 1/2$ for direct and $n = 2$ for indirect zone transition. Except for the Raman spectrometer (which was calibrated using the Raman scattering line of crystalline silicon at 520 cm^{-1}), all the other tools (electron microscope, spectral instruments and the specific surface analyzer) had valid calibration certificates.

2.3. Photocatalytic Activity Testing

The photocatalytic activity of the samples was assessed via the decomposition of aqueous solutions of the well-known model organic pollutant rhodamine B (Rh B). A solution of Rh B dye with a concentration of 5×10^{-6} M (30 mL) was irradiated with LEDs with λ = 375 nm (50 mW), 410 nm (320 mW) and 470 nm (480 mW), while the catalyst loading was 0.5 mg/mL. The power of the LED emission was determined using a wavelength-calibrated PD300UV semiconductor detector (200–1065 nm) from Ophir, Israel. The dispersion was first stirred in the dark for 1 h to establish adsorption–desorption equilibrium. The change in the Rh B concentration during irradiation was determined using a Cary 100SCAN spectrophotometer (Varian, Belrose, Australia), with the relative error of the optical density determination from the absorption spectra not exceeding 3%. The first order reaction rate constant k was calculated from the slope angle from the following dependence graph:

$$\ln(C_0/C) = kt, \quad (2)$$

where C_0 is the initial and C the current concentration of the dye and t is the reaction time.

In the photocatalytic experiment with selective radical scavengers, isopropyl alcohol (IPA, as a hydroxyl radical scavenger), p-benzoquinone (BQ, as a superoxide radical scavenger) and disodium ethylenediaminetetraacetate dihydrate (EDTA, as a photohole scavenger) were used. They were added as 0.12 mL of IPA, 4 mg of BQ or 3 mg of EDTA to 30 mL of tested solution.

We also carried out an experiment on the selective photooxidation of an aqueous solution of 5-hydroxymethylfurfural. Photooxidation of HMF is a new direction in green technologies and biomass processing. The experiments with HMF were carried out with a concentration of 0.01 M (100 mL) under LED irradiation with λ = 375 nm (2 W). The solution was purged with ambient air, and the reaction took place under atmospheric pressure and at room temperature. The catalyst loading was 1 mg/mL. Similar to Rh B, the reaction mixture with HMF was first kept for 1 h in the dark. During irradiation with LEDs, samples were taken and analyzed via high-performance liquid chromatography (HPLC) using a Prominence-i LC-2030C chromatograph (Shimadzu, Kyoto, Japan). The Rezex ROA-Organic Acid H+ (8%) LC column and 0.025 M H_2SO_4 eluent, as well as a PDA detector, were used for the separation and registration of the components. Reference solutions with HMF, 5-hydroxymethyl-2-furancarboxylic acid (HMFCA), 2,5-furandicarboxylic acid (FDCA), 2,5-diformylfuran (DFF), and 5-formyl-2-furancarboxylic acid (FFCA) were used to calibrate the detector, with the compound concentrations being determined from the peak areas.

The analysis was carried out at an eluent flow rate of 0.8 mL/min and an injection volume of 10 μL. Prior to the analysis, the 50 μL aliquot taken was diluted with 1 mL of 0.0125 M H_2SO_4. The HMF conversion, X(HMF), product yield, $Y(i)$, and selectivity, $S(i)$,

as well as the carbon balance, B, were calculated based on the concentrations determined via HPLC:

$$X(\text{HMF}) = \frac{C(\text{HMF})_0 - C(\text{HMF})}{C(\text{HMF})_0} \times 100\%, \quad (3)$$

$$S(i) = \frac{C(i)}{C(\text{HMF})_0 - C(\text{HMF})} \times 100\%, \quad (4)$$

where $C(\text{HMF})_0$ and $C(\text{HMF})$ are initial and current HMF concentrations (in mol/L), $C(i)$ is the current concentration of a ith product (in mol/L), and i = HFCA, FDCA, DFF, and FFCA. The error in determining the concentration of the initial HMF and its photooxidation products for the selected calibration range was no more than 15 rel. %.

2.4. Electrochemical Activity Testing

To fabricate working electrodes for the electrochemical tests, 34 mg of nanomaterial was suspended in a solution containing 0.5% Nafion (150 μL) and ethanol (75 μL). The obtained dispersion was sonicated and homogenized, after which the slurry (20 μL) was deposited onto a fluorine-tin oxide (FTO) glass substrate via the drop-casting method and then dried at room temperature.

All the electrochemical experiments were performed on an electrochemical workstation CHI-660E (CH Instruments, Bee Cave, TX, USA) in a standard three-electrode setup with a working electrode, an Ag/AgCl (1 M KCl) reference electrode, and a carbon counter electrode.

The transient photocurrent response was carried out in 0.1 M Na_2SO_4 aqueous solution under periodic On/Off light pulses of 10 s (λ = 375 nm) and applying potential biases equal to the open circuit potential of the cell. Prior to the measurements, the electrolyte was bubbled with Ar for 10 min to remove the dissolved oxygen.

The electrochemical impedance spectroscopy (EIS) measurements were performed under dark conditions in 5 mM potassium ferro- and ferricyanide solution, $K_4[Fe(CN)_6]^{3-/4-}$, with 0.1 M $NaNO_3$ and applying 0.2 $V_{Ag/AgCl}$ potential in a frequency range of 0.1 Hz to 10^6 Hz for an amplitude of 10 mV. ZView 3.5g software (ZView Inc., Huntington Beach, CA, USA) was used for the equivalent circuit modeling.

3. Results and Discussion

3.1. Characterization of Particle Structure and Morphology

Based on the XRD patterns presented in Figure 1, sample Bi_2O_3 produced via laser ablation in air consisted of the β-Bi_2O_3 phase (PDF-4 #04-015-6851). Sample BSO, prepared via laser ablation in water and then annealed, is represented predominantly by the $Bi_{12}SiO_{20}$ phase (PDF-4 #04-007-2767), with trace amounts (~1%) of the bismuth metasilicate phase Bi_2SiO_5 (PDF-4 #00-036-0287). When obtaining NC particles of β-Bi_2O_3/$Bi_{12}SiO_{20}$, no new phases were found to form, as only β-Bi_2O_3 and sillenite phases were identified in the final samples. Along with the change in the mass ratio of the β-Bi_2O_3/$Bi_{12}SiO_{20}$ in the resulting composites, a change in the volume ratio of the content of the corresponding β-Bi_2O_3 phases was also observed.

Figure 2a exhibits TEM images of sample Bi_2O_3. The sample is seen to consist mainly of spherical nanoparticles whose average sizes lie in the range from 8 to 27 nm, also containing a small amount of somewhat larger particles with sizes up to 50 nm. The specific surface area of sample β-Bi_2O_3 is S_{sp} = 44 m^2/g. Sample BSO is mainly represented by round particles of an irregular shape (Figure 2b) and a few hundred nm in size, the presence of which can be explained by the sintering of smaller ones during annealing at 600 °C. There are also smaller particles (below 100 nm) in this sample, close to spherical, which are located on the surface of the larger round ones. Sample BSO has a small specific surface S_{sp} << 1 m^2/g, which is also explained by the effect of temperature annealing. In the composite samples, small particles of β-Bi_2O_3 are seen in Figure 2c to cover (decorate) the surface of the larger BSO particles quite uniformly.

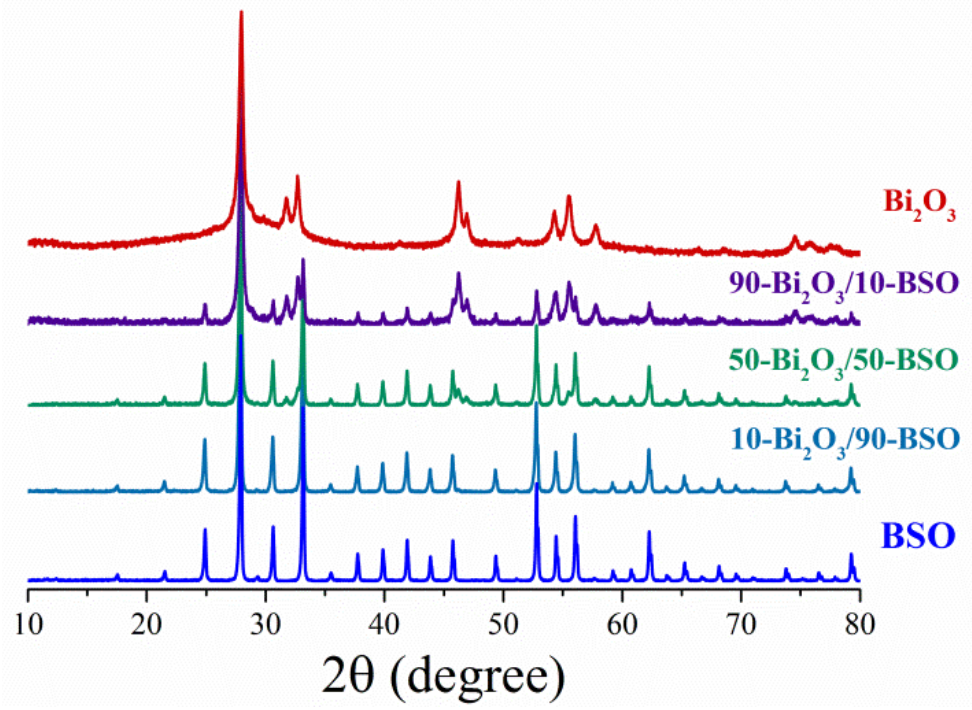

Figure 1. XRD patterns of samples β-Bi_2O_3 and $Bi_{12}SiO_{20}$, and their comparison with three Bi_2O_3/$Bi_{12}SiO_{20}$ composites.

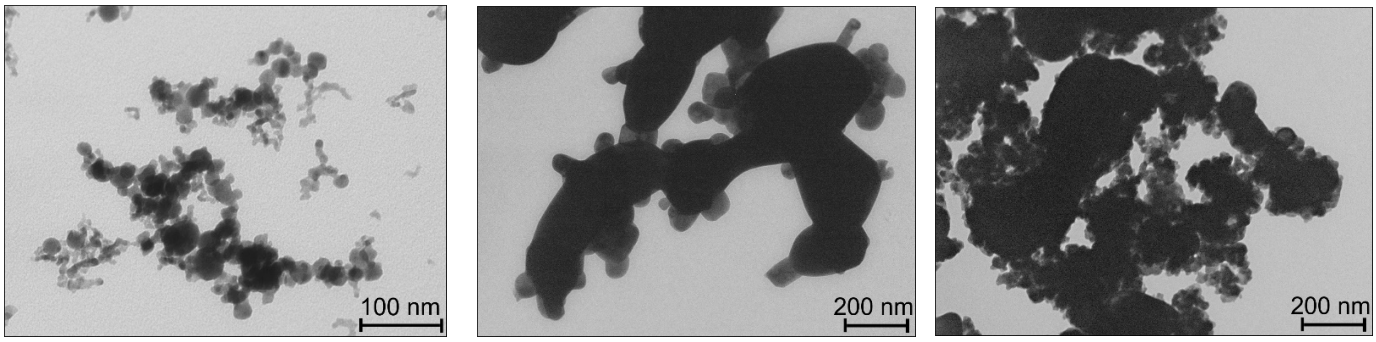

(**a**) (**b**) (**c**)

Figure 2. TEM images of samples Bi_2O_3 (**a**), BSO (**b**), and β-Bi_2O_3/$Bi_{12}SiO_2$ (**c**). The composite in panel (**c**) has its Bi_2O_3/$Bi_{12}SiO_2$ ratio equal to 50:50.

The XRD results were found to correlate with the vibrational spectroscopy data. In the FTIR spectrum of sample Bi_2O_3 (Figure 3a), a set of structureless vibrational bands are observed in the region from 400 to 650 cm^{-1}. In accordance with work [50], this region is characterized by vibrations of the Bi–O bond. A low-intensity band with a maximum at 814 cm^{-1} corresponds to the characteristic vibrations of NO^{3-} groups [51], which are present on the surface of Bi_2O_3 particles. This was previously reported for particles obtained via ablation in atmospheric air [48,49]. All the bands of the FTIR spectrum of sample BSO (Figure 3a) are in good agreement with the previously reported spectra for $Bi_{12}SiO_{20}$ [33]. For example, the strong band at ~825 cm^{-1} is due to absorption via the stretching vibration mode of Bi–O–Si bonds. The IR spectrum of NC particles exhibits vibrations inherent to both bismuth oxide and sillenite. And in a sample with a high content of beta oxide, sample 90-Bi_2O_3/10-BSO, vibrations of the NO^{3-} group can still be observed next to those of Bi–O–Si (a double band with maxima at ~814 and ~830 cm^{-1}).

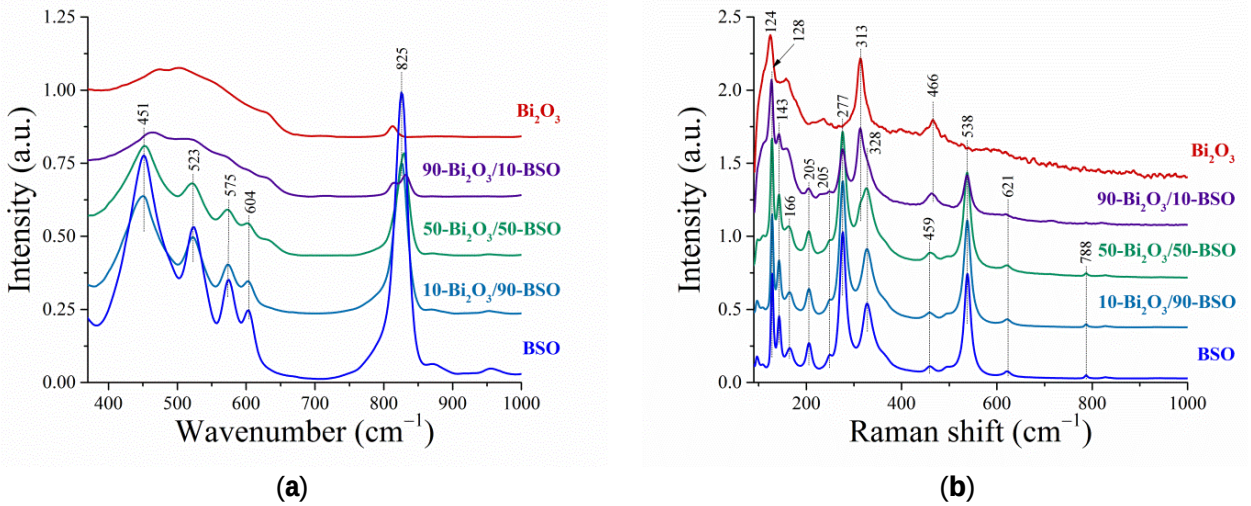

Figure 3. FTIR (**a**) and Raman shift (**b**) spectra of composite β-Bi_2O_3/$Bi_{12}SiO_{20}$ samples with different Bi_2O_3/$Bi_{12}SiO_{20}$ ratios.

All the main bands seen in the Raman spectrum of Bi_2O_3 at 124, 313, and 466 cm^{-1} belong to vibrations of the Bi–O phase of tetragonal β-Bi_2O_3 [52], while in the Raman spectrum of the BSO sample, all the identified bands belong to vibrations characteristic of $Bi_{12}SiO_{20}$ [33,53]. Correspondingly, the spectra of the composite β-Bi_2O_3/$Bi_{12}SiO_{20}$ particles show vibrations related to both β-Bi_2O_3 and $Bi_{12}SiO_{20}$ (Figure 3b).

3.2. Optical Properties of NC Particles

The UV-Vis absorbance of the samples obtained by converting the DRS measurements using the Kubelka–Munk function is presented in Figure 4. Sample BSO is seen in Figure 4a to have an absorption band edge in the region of 360–450 nm, which is consistent with the literature data for $Bi_{12}SiO_{20}$ [36,54]. Estimation of the band gap using the Tauc method for a direct gap transition provides a value of ~3.25 eV. It should be noted that the literature data on the spectral characteristics of sillenite are very different (for instance, the values of E_g were reported to be within the range 2.3–3.3 eV). This can be explained by the unique features of this semiconductor, i.e., the presence of traps in its band gap, and its photorefractive properties, as noted above in the introduction.

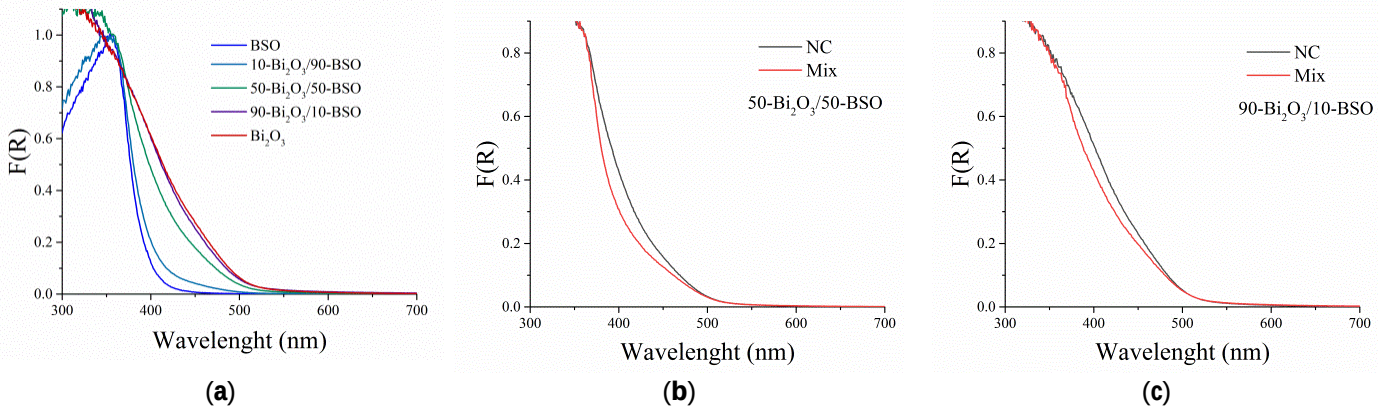

Figure 4. (**a**) UV-Vis spectra of β-Bi_2O_3/$Bi_{12}SiO_{20}$ composites and samples Bi_2O_3 and BSO. (**b**) Comparison of β-Bi_2O_3/$Bi_{12}SiO_{20}$ composite and Bi_2O_3–BSO mixture (both having Bi_2O_3/$Bi_{12}SiO_{20}$ of 50:50 by mass). (**c**) Comparison of β-Bi_2O_3/$Bi_{12}SiO_{20}$ composite and Bi_2O_3–BSO mixture (both having Bi_2O_3/$Bi_{12}SiO_{20}$ of 90:10 by mass).

The edge of the absorption band of sample Bi_2O_3 lies in the longer wavelength region and extends to ~530 nm (Figure 4a), which corresponds well to the spectrum of β-Bi_2O_3 [55]. The flatter slope of the edge of the absorption band of this sample with respect to that of sample BSO confirms that β-Bi_2O_3 is an indirect gap semiconductor. The Tauc bandgap estimate corresponds to most of the literature data, being 2.4 eV [27,55]. The absorption spectra of NC powders are seen to be intermediate between those of samples BSO and β-Bi_2O_3; and an increase in the content of β-Bi_2O_3 leads to a corresponding long-wave shift of the spectrum. No E_g assessment of the composite samples was carried out, because the Tauc method should be used primarily for single-phase samples.

In addition to studying the spectra of both the single-phase and NC samples, we carefully prepared homogeneous mixtures of sillenite with β-Bi_2O_3 and compared them with the corresponding NC powders with the same ratio of components. The comparison showed that the spectra of nanocomposite particles shifted toward longer wavelengths (Figure 4b,c), which indicates a strong interaction between the different phases and confirms the formation of NCs.

3.3. Photocatalytic Properties of NC Particles

3.3.1. Decomposition of Rh B

The results of the Rh B photodecomposition in the presence of the individual single-phase samples Bi_2O_3 and BSO, as well as their mechanical mixture and their composites, are presented in Figure 5 and in Table 1. Rhodamine B is known as a persistent dye, and its decomposition under irradiation with 375 nm and without any photocatalyst was found to be no more than 1% after 8 h, as was previously shown in our report [41]. As a result of photocatalysis, the aromatic structure of the dye was effectively destroyed, which was accompanied by the discoloration of the tested solutions. The typical bleaching dynamics observed for all the samples and for all the irradiation wavelengths are shown in Figure 5a. When Rh B is destroyed, a hypsochromic shift in the absorption maximum is seen, which is caused by the formation of an N-deethylated intermediate, rhodamine 110 [46,56,57]. Then, the resultant intermediate product was also efficiently degraded by our photocatalysts. The absorbance was observed to decrease in the whole spectral range, including the UV region, indicating an efficient decomposition of the aromatic structure of the dye.

The efficiency of the Rh B destruction upon excitation at 375 nm for the single-phase catalysts Bi_2O_3 and BSO is seen to be close, with their rate constant being 0.043 and 0.031 min^{-1}, respectively (Table 1). The interaction between the phases in the composite particles leads to an increase in the efficiency of the catalyst. At the optimal Bi_2O_3/BSO ratio of 50:50, the rate constant was found to increase to 0.1 min^{-1}, i.e., more than two times when compared with that for the best single-phase semiconductor β-Bi_2O_3. Similar results were observed upon excitation with wavelengths of 410 and 475 nm, although the most optimal Bi_2O_3/BSO ratio in the composite was 90:10. This is related to the weak absorption of BSO in the visible region of the spectrum.

We also investigated the photocatalytic properties of conventional mixtures of single-phase powders prepared with the same ratios as their corresponding NCs (Table 1). A weak synergistic effect was observed for such mixtures, while overall their activity was almost two times smaller than that of composites of similar composition. Nevertheless, this result suggests that “pure” and “soft” nanoparticles produced by laser are prone to interact easily.

The increase in photocatalytic activity for the composite material can be attributed to the better separation of photogenerated charge carriers, which in our case implies the formation of type II heterojunctions between β-Bi_2O_3 and $Bi_{12}SiO_{20}$. However, both of these semiconductors are typically *p*-type. Therefore, based on their energy schemes, and taking into account the experimentally determined E_g values, type I heterojunctions were more likely to form upon contact. This implies that the observed increase in the catalytic activity of the prepared NCs requires explanation.

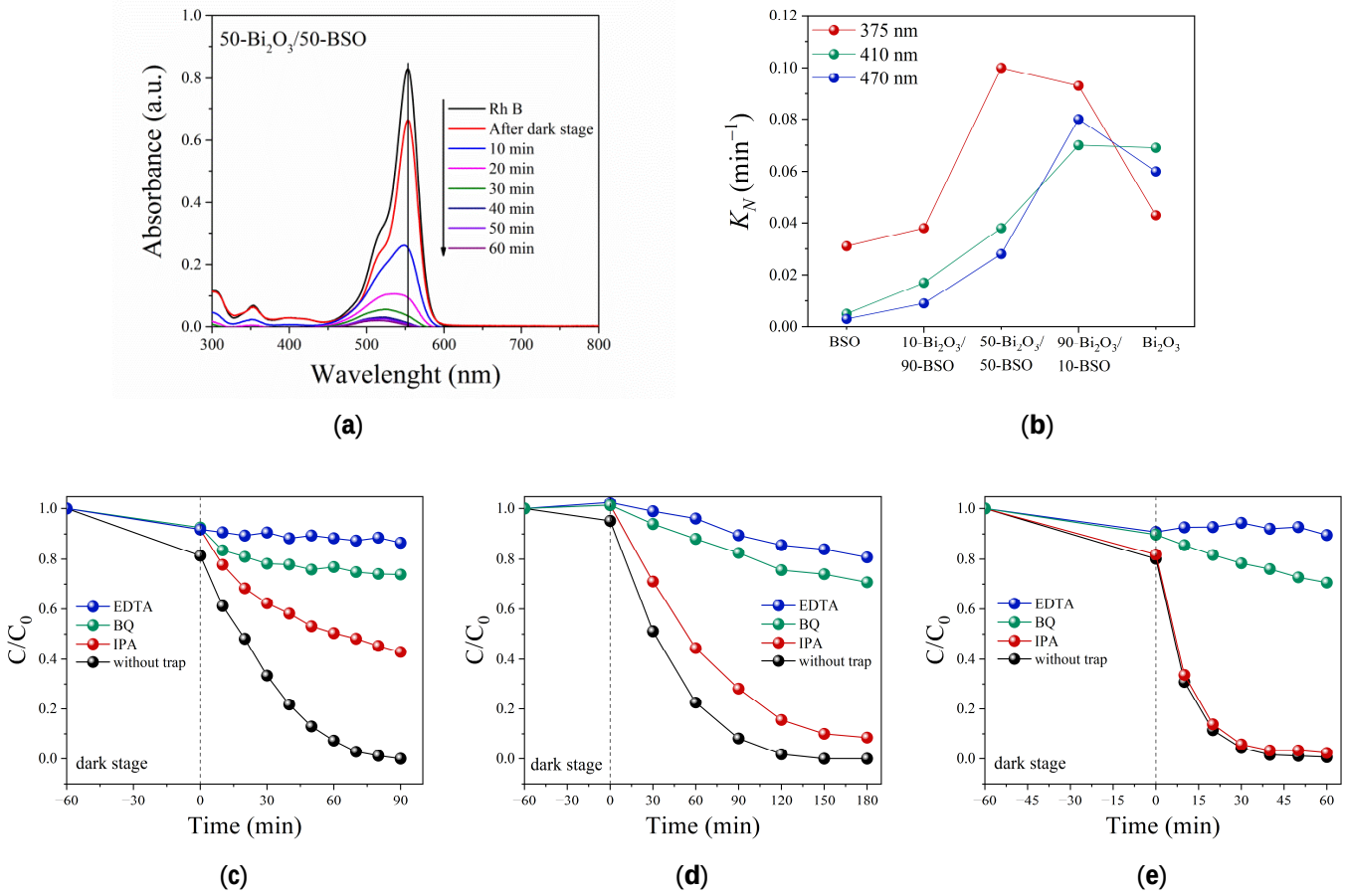

Figure 5. (**a**) Typical photodecomposition dynamics of Rh B in the presence of a composite catalyst (with the ratio of 50:50). (**b**) Reaction rate constant of Rh B photodecomposition versus the composition of a catalyst, as found for three excitation wavelengths, and comparison of photocatalytic activity of catalysts Bi_2O_3 (**c**), BSO (**d**), and 50-Bi_2O_3/50-BSO (**e**) in the course of the degradation of Rh B with or without the addition of IPS, BQ, and EDTA.

Table 1. Photodecomposition rate constants for Rhodamine B.

Sample	K_N, min^{-1}		
	λ = 375 nm	λ = 410 nm	λ = 470 nm
BSO	0.031	0.005	0.003
10-Bi_2O_3/90-BSO	0.038	0.017	0.009
50-Bi_2O_3/50-BSO	0.100	0.038	0.028
50-Bi_2O_3/50-BSO (mix)	0.053	-	-
90-Bi_2O_3/10-BSO	0.093	0.070	0.080
10-Bi_2O_3/90-BSO (mix)	0.057	-	-
Bi_2O_3	0.043	0.069	0.060

To establish the possible mechanisms of Rh B photodegradation, a test using selective radical scavengers that bind individual active species and prevent their participation in photocatalytic processes (the so-called spin-trapping method [58]) was carried out. As a result, it was found that for all the materials an important role in photo-stimulated processes of Rh B destruction is played by oxidative reactions that involve $^{\bullet}O_2^-$ active species (Figure 5c–e). The addition of a selective scavenger of superoxide radicals, BQ, to the medium led to a decrease in the activity of all the catalysts. At the same time, the role of

hydroxide radicals in dye photodetection was found to be much smaller. When a selective absorber of hydroxide radicals, IPA, was added, the catalytic activity of the tested catalysts did not decrease significantly, especially for the composite sample. This may prove that the energy of the holes is not sufficient for the efficient formation of •OH radicals. In this case, one can assume the direct oxidative decomposition of Rh B by means of photoholes (see the results of test with the selective hole absorber EDTA in Figure 5c–e).

The stability of the photocatalysts in the N-deethylation process was evaluated during Rh B decomposition under irradiation by LED with a wavelength of 375 nm (Figure 6). During the first cycle, the complete N-deethylation of Rh B in the presence of the catalysts BSO, Bi_2O_3 and 50-Bi_2O_3/50-BSO composite was found to occur in 3, 2 and 1 h, respectively. As seen in Figure 6a, sample BSO remained stable over five cycles. For comparison, the photocatalytic efficiency of sample Bi_2O_3 started to decrease slightly after three cycles (Figure 6b), which is due to the reduction of bismuth. At the same time, the composite sample demonstrated a monotonic decrease in its efficiency with each cycle (see Figure 6c). Nevertheless, even after five cycles of operation, its photocatalytic activity was still superior to that of samples BSO and Bi_2O_3 (Figure 6c). The observed decrease in catalytic efficiency during the cyclic stability experiments is likely to indicate a gradual disruption of the contact between the two semiconductor components of the composite. As a result, this leads to the gradual decay of the heterostructure that was obtained using such a mild mechanical method.

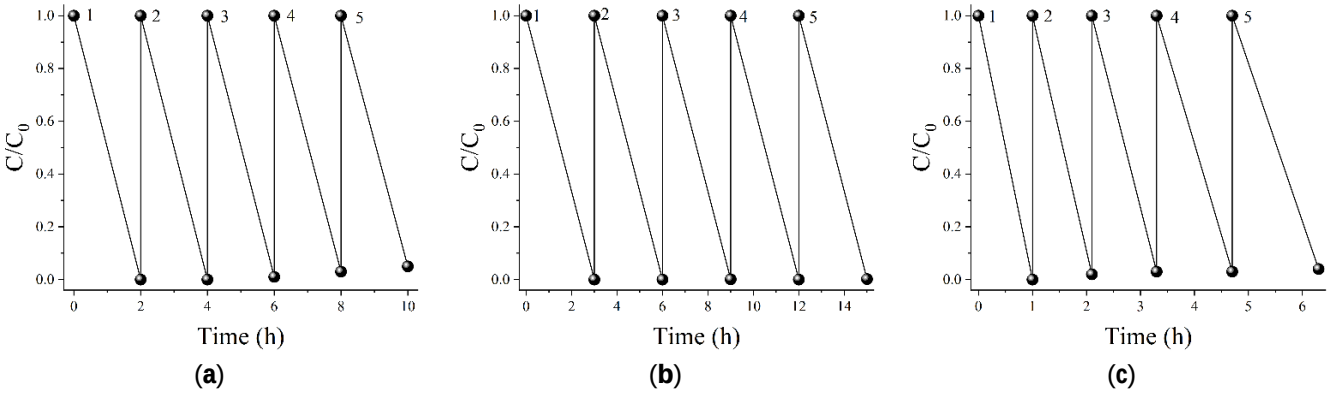

Figure 6. Cyclic stability curves of samples Bi_2O_3 (**a**), BSO (**b**), and 50-Bi_2O_3/50-BSO (**c**) as they decompose Rh B under irradiation with λ = 375 nm.

3.3.2. Selective Oxidation of HMF

The results obtained from the photooxidation of HMF are presented in Figure 7. In the absence of a catalyst, no changes are seen in the HMF solution. The absorption peak of HMF is known to be about 280 nm, and the HMF molecule does not absorb energy in the region longer than 320 nm [59]. Figure 7a shows schematically the pathways of the selective oxidation of HMF to various products, and Ref. [5] discusses in detail possible reactions involving photogenerated charge carriers and active particles formed in the medium. Under the used conditions, sample BSO demonstrated a very low conversion level of HMF (~2%), which is why the data had a large error and are not presented in this work. In the presence of samples Bi_2O_3 and 50-Bi_2O_3/50-BSO, the 5-HMF conversion increased with the irradiation time to 5.8 and 7.2%, respectively. In both cases, the main product of the selective photooxidation of HMF was 2,5-diformylfuran (DFF), while some amounts of 2,5-furandicarboxylic acid (FDCA) and 5-hydroxymethyl-2-furancarboxylic acid (HMFCA) were also observed. The DFF selectivity in the presence of sample Bi_2O_3 changed from 8.6 to 3.5%, with a maximum observed after 2 h of irradiation at a HMF conversion of 1.3% (Figure 7b). For composite sample 50-Bi_2O_3/50-BSO, the DFF selectivity is seen in Figure 7c to increase remarkably and vary from 8 to 7.7%, passing through a maximum of 10.6% at a HMF conversion of 4.1%. At the same conversion (~5%), the selectivity toward DFF for sample 50-Bi_2O_3/50-BSO was significantly higher (10.3%) than that for sample

Bi_2O_3 (4.2%). Note that the experiments were carried out in distilled water and at a low irradiation power; changing the pH by adding an alkali agent, such as $NaHCO_3$, and increasing the LED power should lead to a significant increase in conversion.

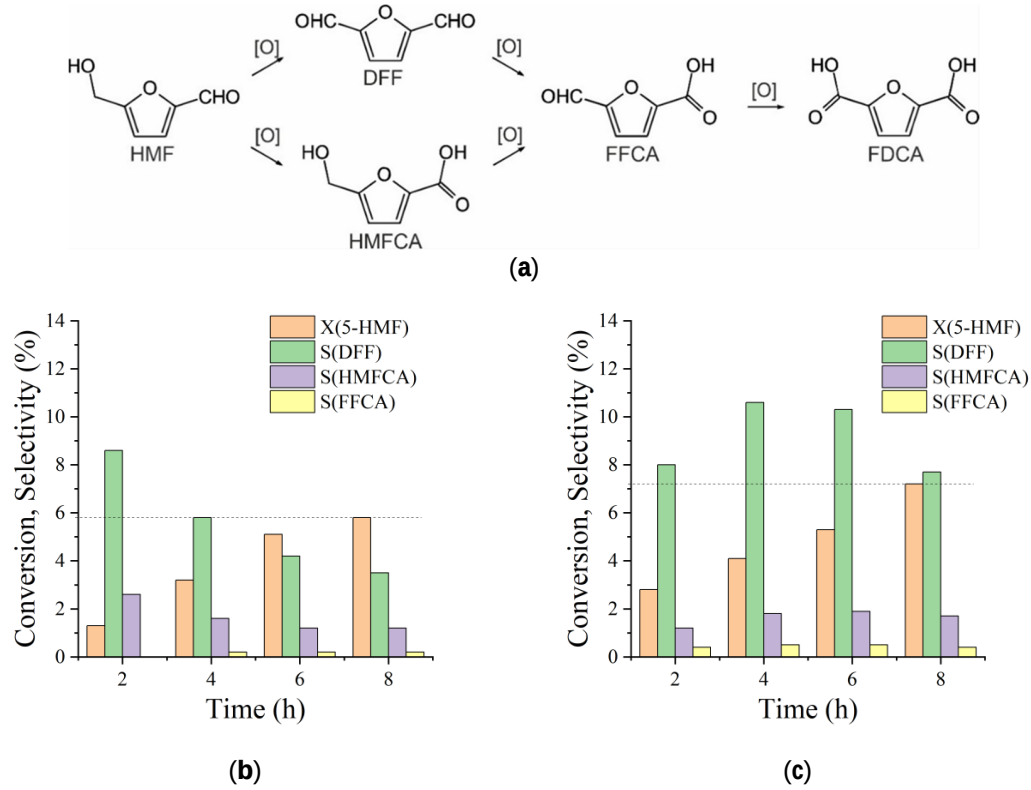

Figure 7. Photocatalytic oxidation of HMF. Reaction route scheme for its oxidation (**a**). Results obtained in the presence of samples Bi_2O_3 (**b**) and 50-Bi_2O_3/50-BSO (**c**).

3.4. Electrochemical Properties of NC Particles

The photocurrent responses of the samples were measured to reveal their photocatalytic activities under irradiation with UV light. The obtained results are seen in Figure 8a to show that all the samples had cathodic behavior, which is characteristic of *p*-type semiconductors [60]. Sample 50-Bi_2O_3/50-BSO had the highest photocurrent response in comparison to samples Bi_2O_3 and BSO, which correlates with the Ph B photodecomposition rate constants at λ = 375 nm shown in Table 1. It is worth mentioning that the *i*–*t* curves had different morphology, which can be associated with various defect states influencing the charge separation processes and, as a result, electron–hole pair lifetime. It can be seen that all the samples demonstrated good durability, with a small decrease in photocurrent density for sample 50-Bi_2O_3/50-BSO, whose peak intensity stabilized after ~1000 s.

EIS measurements were performed in order to understand the charge-transport processes occurring in the prepared samples (Figure 8b). It is clearly seen that the Nyquist plots of samples Bi_2O_3 and BSO display two semicircles, while an additional part of semicircle observed at low frequencies characterizes sample 50-Bi_2O_3/50-BSO. Such a complex Nyquist plot reveals an additive effect of each component of the composite. In the high frequency region, small semicircles are found, which can be ascribed to the resistivity of the FTO substrate. The most important factor for the photocatalytic performance of materials is the charge transfer resistivity R_{ct}, which is associated with the radius of the second semicircle. Composite 50-Bi_2O_3/50-BSO is seen to provide significantly lower impedance values for its semicircle, which correlates with its photocurrent response. The change in the arc radius of the tested samples follows the sequence: 50-Bi_2O_3/50-BSO < BSO < Bi_2O_3. Despite the fact that sample BSO demonstrates a lower resistivity than sample Bi_2O_3, they both show comparable photocurrent intensities. In this regard, structural defects, heterojunctions,

surface states, working conditions (e.g., presence of organic molecules in the solution) and other factors should also be taken into consideration to understand better the photocatalytic properties of the tested materials.

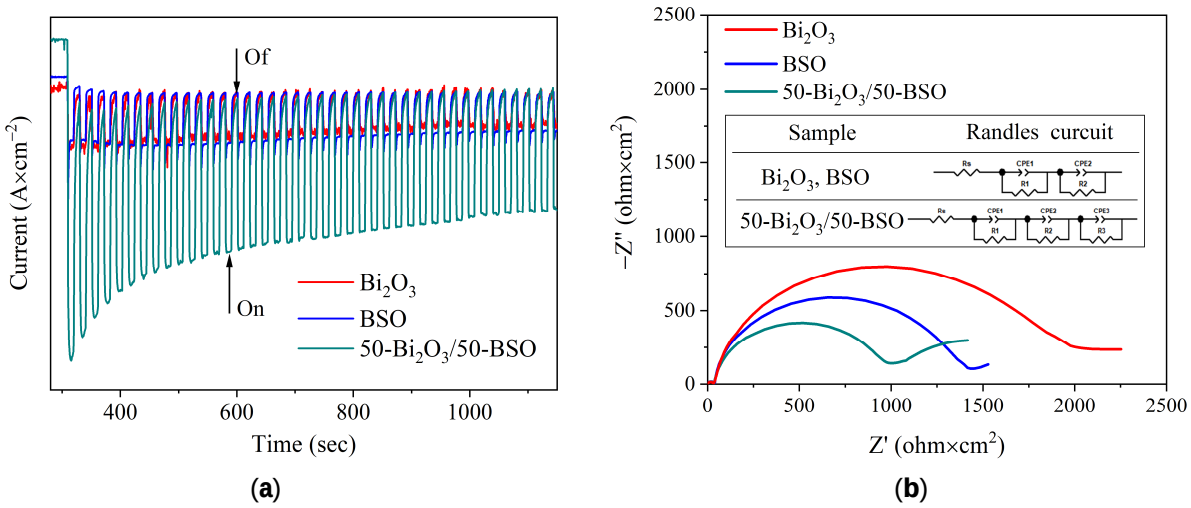

Figure 8. The *i–t* curves of the samples under UV irradiation with LED with λ = 375 nm (**a**); and Nyquist plots (**b**).

4. Discussion

To explain the increase in the catalytic activity of the novel Bi_2O_3/BSO NCs, based on the results obtained and the literature data on the energy structure and optical properties of the corresponding semiconductors, we considered the following schematic diagram of the energy states and separation of the electron–hole pairs (see Figure 9).

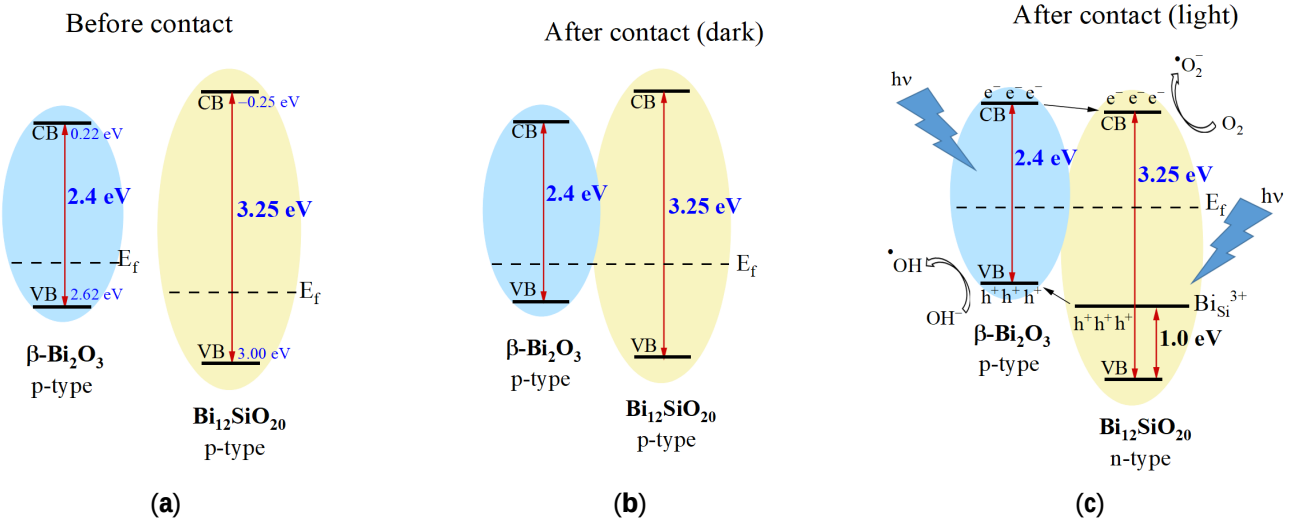

Figure 9. Schematic diagram of the energy states and separation of the electron–hole pairs in individual semiconductor NPs (**a**) and on a β-Bi_2O_3/$Bi_{12}SiO_{20}$ heterojunction in the dark (**b**) and under the influence of light (**c**).

Since both initial single-phase materials are *p*-type semiconductors [30,35], as shown in Figure 9a, upon contacting, they form type I heterojunctions (Figure 9b). Typically, this configuration of energy levels formed in NC particles does not lead to improved catalytic properties, since it does not contribute to better charge separation, and the redox potential of such a system, in general, is not better than the redox ability of the narrowest bandgap

component of the heterostructure. All this is owing to the relative position of the energy levels of electrons and holes in such particles with heterojunctions (Figure 9b).

Increased photocatalytic efficiency can be achieved through better charge separation within the particle, which is realized in type II heterojunction composite particles. In this case, the redox ability of the heterostructure II is lower than the redox ability of each individual component included in it. In such a structure, a compromise is necessary between thermodynamic and kinetic factors. The second well-known approach is the creation of a z-scheme, where not only effective charge separation occurs but also the redox ability of the heterostructure in relation to its constituent individual semiconductors increases [15].

However, sillenite, which is part of our NC particles, has completely unique properties due to the special defect structure of its bandgap [36,37,61]. Upon photoexcitation, effective population of the electron donor center Bi_{Si}^{3+} + h^+ (which is a trap level located ~1 eV above the VB) occurs [36]. As a result, $Bi_{12}SiO_{20}$ exhibits photorefractive properties, and the conductivity changes abruptly from *p*- to *n*-type [37,62]. Hence, after irradiation, the heterostructure can be presented as shown in Figure 9c. In this light, the operation of the photocatalyst can be described in terms of a type II heterojunction, which explains the increase in the photocatalytic activity of the NC particles prepared in this study.

It should be noted that a slight decrease in the thermodynamic characteristics of the system in type II heterostructures can have a dramatic effect on the processes of photocatalytic water splitting or CO_2 reduction for the production of solar fuels [63]. In the case of dye decomposition, a slight decrease in the redox potential of the heterostructure may not have a significant effect on the efficiency, which increases due to the better charge separation, i.e., process kinetics (Figure 5b). And for processes such as the photooxidation of HMF, this can be an effective way to change the thermodynamics of the process, permitting control of the reaction paths and the selectivity of the yield of certain products, as can be seen in Figure 7.

5. Conclusions

The present work implements a simple method for the preparation of β-Bi_2O_3/$Bi_{12}SiO_{20}$ nanocomposites from individual single-phase semiconductor nanoparticles generated via pulsed laser ablation. Being "pure" and "soft", such nanoparticles easily interact when ground as a mixture of their powders in a mortar, which leads to the formation of composite particles. Using a set of methods, it was shown that the approach used to obtain the composite material provided a homogeneous distribution of the phases of the composite components and their interaction at the interface, which was necessary for the creation of a heterostructure.

The resulting composites were demonstrated to exhibit excellent photocatalytic properties in the decomposition of Rh B, which were superior to those of both individual materials used as components. The optimal ratio of the components in the obtained composites that provides a significant increase in photocatalytic activity was established. This was achieved due to the formation of a type II heterojunction in the produced composite structures. Both materials in the composite are *p*-type semiconductors and, under normal conditions, they should form a type I heterostructure. However, due to the unique properties of sillenite (under photoexcitation, the trap levels in its bandgap are populated, which results in a change of conductivity from *p*- to *n*-type), the newly prepared composite is believed to work as a type II heterostructure, which explains the results obtained in this work. Cyclic stability tests showed that the heterostructure obtained using this mild mechanical method degrades with time, and thus further studies on its stabilization are required.

The prepared Bi_2O_3/BSO composite also exhibited catalytic activity in the selective photooxidation of HMF, which is an important direction in modern green catalytic technologies. This makes such materials promising, and further research will aim at studying this process in order to control the conversion efficiency and increase the selectivity of the yield of useful products.

Author Contributions: Conceptualization, V.A.S. and O.V.V.; methodology, V.A.S.; validation, E.A.G., E.D.F. and O.V.V.; formal analysis, S.A.K.; investigation, A.G.G., T.S.K., E.A.G., E.D.F. and V.A.S.; data curation, S.A.K.; writing—original draft preparation, A.G.G. and V.A.S.; writing—review and editing, E.A.G., E.D.F., S.A.K., O.V.V. and V.A.S.; visualization, A.G.G. and T.S.K.; supervision, S.A.K.; project administration, V.A.S.; funding acquisition, O.V.V. All authors have read and agreed to the published version of the manuscript.

Funding: This work was supported by the Russian Science Foundation, grant no. 19-73-30026.

Data Availability Statement: The data presented in this study are available on request from the corresponding authors.

Acknowledgments: The studies (Raman, FTIR, UV-Vis spectroscopy and TEM) were carried out using the equipment of the Tomsk Regional Core Shared Research Facilities Center of National Research Tomsk State University.

Conflicts of Interest: The authors declare no conflicts of interest.

References

1. Yang, X.; Chen, Z.; Zhao, W.; Liu, C.; Qian, X.; Zhang, M.; Wei, G.; Khan, E.; Ng, Y.H.; Ok, Y.S. Recent advances in photodegradation of antibiotic residues in water. *Chem. Eng. J.* **2021**, *405*, 126806. [CrossRef]
2. Rafiq, A.; Ikram, M.; Ali, S.; Niaz, F.; Khan, M.; Khan, Q.; Maqbool, M. Photocatalytic degradation of dyes using semiconductor photocatalysts to clean industrial water pollution. *J. Ind. Eng. Chem.* **2021**, *97*, 111–128. [CrossRef]
3. Subhiksha, V.; Kokilavani, S.; Khan, S.S. Recent advances in degradation of organic pollutant in aqueous solutions using bismuth based photocatalysts: A review. *Chemosphere* **2022**, *290*, 133228. [CrossRef] [PubMed]
4. Meng, Y.; Yang, S.; Li, H. Electro- and photocatalytic oxidative upgrading of biobased 5-hydroxymethylfurfural. *ChemSusChem* **2022**, *15*, e202102581. [CrossRef] [PubMed]
5. Sun, H.; Xu, R.; Jia, X.; Liu, Z.; Chen, H.; Lu, T. Recent advances in the photocatalytic oxidation of 5-hydroxymethylfurfural to 2,5-diformylfuran. *Biomass Convers. Biorefinery* **2023**. [CrossRef]
6. Zhang, Q.; Zhang, H.; Gu, B.; Tang, Q.; Cao, Q.; Fang, W. Sunlight-driven photocatalytic oxidation of 5-hydroxymethylfurfural over a cuprous oxide-anatase heterostructure in aqueous phase. *Appl. Catal. B* **2023**, *320*, 122006. [CrossRef]
7. Nam, J.-W.; Pham, V.N.; Ha, J.M.; Shin, M.; Lee, H.; Youn, Y.-S. Photocatalysis of Cr- and Fe-doped CeO_2 nanoparticles to selective oxidation of 5-hydroxymethylfurfural. *Nanomaterials* **2023**, *13*, 44. [CrossRef]
8. Davis, K.A.; Yoo, S.; Shuler, E.W.; Sherman, B.D.; Lee, S.; Leem, G. Photocatalytic hydrogen evolution from biomass conversion. *Nano Converg.* **2021**, *8*, 6. [CrossRef]
9. Low, J.; Dai, B.; Tong, T.; Jiang, C.; Yu, J. In situ irradiated X-ray photoelectron spectroscopy investigation on a direct Z-scheme TiO_2/CdS composite film photocatalyst. *Adv. Mater.* **2019**, *31*, 1802981. [CrossRef]
10. Lee, K.M.; Lai, C.W.; Ngai, K.S.; Juan, J.C. Recent developments of zinc oxide based photocatalyst in water treatment technology: A review. *Water Res.* **2016**, *88*, 428–448. [CrossRef]
11. Liu, Y.; Zhang, Q.; Xu, M.; Yuan, H.; Chen, Y.; Zhang, J.; Luo, K.; Zhang, J.; You, B. Novel and efficient synthesis of Ag-ZnO nanoparticles for the sunlight-induced photocatalytic degradation. *Appl. Surf. Sci.* **2019**, *476*, 632–640. [CrossRef]
12. Wang, K.; Yoshiiri, K.; Rosa, L.; Wei, Z.; Juodkazis, S.; Ohtani, B.; Kowalska, E. TiO_2/Au/TiO_2 plasmonic photocatalyst with enhanced photocatalytic activity and stability under visible-light irradiation. *Catal. Today* **2022**, *397–399*, 257–264. [CrossRef]
13. Hasija, V.; Raizada, P.; Sudhaik, A.; Sharma, K.; Kumar, A.; Singh, P.; Jonnalagadda, S.B.; Thakur, V.K. Recent advances in noble metal free doped graphitic carbon nitride based nanohybrids for photocatalysis of organic contaminants in water: A review. *Appl. Mater. Today* **2019**, *15*, 494–524. [CrossRef]
14. Ahmad, I.; Zou, Y.; Yan, J.; Liu, Y.; Shukrullah, S.; Naz, M.Y.; Hussain, H.; Khan, W.Q.; Khalid, N.R. Semiconductor photocatalysts: A critical review highlighting the various strategies to boost the photocatalytic performances for diverse applications. *Adv. Colloid Interface Sci.* **2023**, *311*, 102830. [CrossRef] [PubMed]
15. Emeline, A.V.; Rudakova, A.V.; Ryabchuk, V.K.; Serpone, N. Recent advances in composite and heterostructured pho-toac-tive materials for the photochemical conversion of solar energy. *Curr. Opin. Green Sustain. Chem.* **2022**, *34*, 100588. [CrossRef]
16. Wang, T.; Zhu, Q.; Huo, C.; Yin, Z.; Shi, Q.; Tao, J.; Su, F.; Cao, S. Constructing flower-like TiO_2/Bi_2O_3 p-n heterojunction with enhanced visible-light photocatalytic performance. *J. Alloys Compd.* **2023**, *950*, 169889. [CrossRef]
17. Goodarzi, N.; Ashrafi-Peyman, Z.; Khani, E.; Moshfegh, A.Z. Recent progress on semiconductor heterogeneous photocatalysts in clean energy production and environmental remediation. *Catalysts* **2023**, *13*, 1102. [CrossRef]
18. Song, Y.; Bao, Z.; Gu, Y. Photocatalytic enhancement strategy with the introduction of metallic Bi: A review on Bi/semiconductor photocatalysts. *Chem. Rec.* **2023**, e202300307. [CrossRef]
19. Wang, Z.; Lin, Z.; Shen, S.; Zhong, W.; Cao, S. Advances in designing heterojunction photocatalytic materials. *Chin. J. Catal.* **2021**, *42*, 710–730. [CrossRef]
20. Low, J.; Jiang, C.; Cheng, B.; Wageh, S.; Al-Ghamdi, A.A.; Yu, J. A Review of Direct Z-Scheme Photocatalysts. *Small Methods* **2017**, *1*, 1700080. [CrossRef]

21. Yuan, D.; Sun, M.; Tang, S.; Zhang, Y.; Wang, Z.; Qi, J.; Rao, Y.; Zhang, Q. All-solid-state $BiVO_4/ZnIn_2S_4$ Z-scheme composite with efficient charge separations for improved visible light photocatalytic organics degradation. *Chin. Chem. Lett.* **2020**, *31*, 547–550. [CrossRef]
22. Rengifo-Herrera, J.A.; Pulgarin, C. Why five decades of massive research on heterogeneous photocatalysis, especially on TiO_2, has not yet driven to water disinfection and detoxification applications? Critical review of drawbacks and challenges. *Chem. Eng. J.* **2023**, *477*, 146875. [CrossRef]
23. Wang, W.; Li, X.; Deng, F.; Liu, J.; Gao, X.; Huang, J.; Xu, J.; Feng, Z.; Chen, Z.; Han, L. Novel organic/inorganic PDI-Urea/BiOBr S-scheme heterojunction for improved photocatalytic antibiotic degradation and H_2O_2 production. *Chin. Chem. Lett.* **2022**, *33*, 5200–5207. [CrossRef]
24. Li, F.; Zhu, G.; Jiang, J.; Yang, L.; Deng, F.; Arramel; Li, X. A review of updated S-scheme heterojunction photocatalysts. *J. Mater. Sci. Technol.* **2024**, *177*, 142–180. [CrossRef]
25. Prabhakar Vattikuti, S.V.; Zeng, J.; Ramaraghavulu, R.; Shim, J.; Mauger, A.; Julien, C.M. High-throughput strategies for the design, discovery, and analysis of bismuth-based photocatalysts. *Int. J. Mol. Sci.* **2023**, *24*, 663. [CrossRef] [PubMed]
26. Sivasubramanian, P.; Chang, J.; Nagendran, S.; Dong, C.; Shkir, M.; Kumar, M. A review on bismuth-based nanocomposites for energy and environmental applications. *Chemosphere* **2022**, *307*, 135652. [CrossRef]
27. Schlesinger, M.; Schulze, S.; Hietschold, M.; Mehring, M. Metastable β-Bi_2O_3 nanoparticles with high photocatalytic activity from polynuclear bismuth oxido clusters. *Dalton Trans.* **2013**, *42*, 1047–1056. [CrossRef]
28. Shu, S.; Wang, H.; Li, Y.; Liu, J.; Liu, J.; Yao, J.; Liu, S.; Zhu, M.; Huang, L. Fabrication of n-p β-Bi_2O_3@BiOI core/shell photocatalytic heterostructure for the removal of bacteria and bisphenol A under LED light. *Colloids Surf. B* **2023**, *221*, 112957. [CrossRef]
29. Shuk, P.; Wiemhöfer, H.-D.; Guth, U.; Göpel, W.; Greenblatt, M. Oxide ion conducting solid electrolytes based on Bi_2O_3. *Solid State Ionics* **1996**, *89*, 179–196. [CrossRef]
30. Hu, R.; Xiao, X.; Tu, S.; Zuo, X.; Nan, J. Synthesis of flower-like heterostructured β-$Bi_2O_3/Bi_2O_2CO_3$ microspheres using $Bi_2O_2CO_3$ self-sacrifice precursor and itsvisible-light-induced photocatalytic degradation of *o*-phenylphenol. *Appl. Catal. B* **2015**, *163*, 510–519. [CrossRef]
31. Huang, Y.; Wei, Y.; Wang, J.; Luo, D.; Fan, L.; Wu, J. Controllable fabrication of Bi_2O_3/TiO_2 heterojunction with excellent visible-light responsive photocatalytic performance. *Appl. Surf. Sci.* **2017**, *423*, 119–130. [CrossRef]
32. Park, S.; Jun, J.; Kim, H.W.; Lee, C. Preparation of one dimensional Bi_2O_3-core/ZnO-shell structures by thermal evaporation and atomic layer deposition. *Solid State Commun.* **2009**, *149*, 315–318. [CrossRef]
33. Wu, Y.; Chang, X.; Li, M.; Hei, X.; Liu, C.; Zhan, X. Studying the preparation of pure $Bi_{12}SiO_{20}$ by Pechini method with high photocatalytic performance. *J. Sol-Gel Sci. Technol.* **2021**, *97*, 311–319. [CrossRef]
34. Weber, M.; Rodriguez, R.D.; Zahn, D.R.T.; Mehring, M. γ-Bi_2O_3—To Be or Not To Be? Comparison of the Sillenite γ-Bi_2O_3 and Isomorphous Sillenite-Type $Bi_{12}SiO_{20}$. *Inorg. Chem.* **2018**, *57*, 8540–8549. [CrossRef]
35. Isik, M.; Surucu, G.; Gencer, A.; Gasanly, N.M. Electronic, optical and thermodynamic characteristics of $Bi_{12}SiO_{20}$ sillenite: First principle calculations. *Mater. Chem. Phys.* **2021**, *267*, 124711. [CrossRef]
36. Oberschmid, R. Absorption Centers of $Bi_{12}GeO_{20}$ and $Bi_{12}SiO_{20}$ crystals. *Phys. Stat. Sol. A* **1985**, *89*, 263–270. [CrossRef]
37. Attard, A.E. Fermi level shift in $Bi_{12}SiO_{20}$ via photon-induced trap level occupation. *J. Appl. Phys.* **1992**, *71*, 933–937. [CrossRef]
38. Zhang, Q.; Ravindra; Xia, H.; Zhang, L.; Zeng, K.; Xu, Y.; Xin, C. Microwave hydrothermal synthesis of a $Bi_2SiO_5/Bi_{12}SiO_{20}$ heterojunction with oxygen vacancies and multiple charge transfer for enhanced photocatalytic activity. *Appl. Surf. Sci.* **2022**, *581*, 152337. [CrossRef]
39. Dadashi, S.; Poursalehi, R.; Delavari, H.H. Formation, gradual oxidation mechanism and tunable optical properties of Bi/Bi_2O_3 nanoparticles prepared by Nd: YAG laser ablation in liquid: Dissolved oxygen as genesis of tractable oxidation. *Mater. Res. Bull.* **2018**, *97*, 421–427. [CrossRef]
40. Hassan, S.S.; Hubeatir, K.A.; Al-Haddad, R.M.S. Characterization and antibacterial activity of silica-coated bismuth (Bi@SiO_2) nanoparticles synthesized by pulsed laser ablation in liquid. *Optik* **2023**, *273*, 170453. [CrossRef]
41. Shabalina, A.V.; Fakhrutdinova, E.D.; Golubovskaya, A.G.; Kuzmin, S.M.; Koscheev, S.V.; Kulinich, S.A.; Svetlichnyi, V.A.; Vodyankina, O.V. Laser-assisted preparation of highly-efficient photocatalytic nanomaterial based on bismuth silicate. *Appl. Surf. Sci.* **2022**, *575*, 151722. [CrossRef]
42. Flores-Castaneda, M.; Camacho-Lopez, S. Si nanoparticle decorated $Bi_2O_2CO_3$ 2D nanocomposite synthesized by femtosecond laser ablation of solids in liquids and aging. *Opt. Laser Technol.* **2023**, *158*, 108891. [CrossRef]
43. Amendola, V.; Amans, D.; Ishikawa, Y.; Koshizaki, N.; Scire, S.; Compagnini, G.; Reichenberger, S.; Barcikowski, S. Room-Temperature laser synthesis in liquid of oxide, metal-oxide core-shells, and doped oxide nanoparticles. *Chem. Eur. J.* **2020**, *26*, 9206–9242. [CrossRef]
44. Goncharova, D.A.; Kharlamova, T.S.; Reutova, O.A.; Svetlichnyi, V.A. Water-ethanol CuO_x nanoparticle colloids prepared by laser ablation: Colloid stability and catalytic properties in nitrophenol hydrogenation. *Colloids Surf. A Physicochem. Eng.* **2021**, *613*, 126115. [CrossRef]
45. Forsythe, R.C.; Cox, C.P.; Wilsey, M.K.; Müller, A.M. Pulsed laser in liquids made nanomaterials for catalysis. *Chem. Rev.* **2021**, *121*, 7568–7637. [CrossRef]

46. Shabalina, A.V.; Golubovskaya, A.G.; Fakhrutdinova, E.D.; Kulinich, S.A.; Vodyankina, O.V.; Svetlichnyi, V.A. Phase and structural thermal evolution of Bi-Si-O catalysts obtained via laser ablation. *Nanomaterials* **2022**, *12*, 4101. [CrossRef]
47. Svetlichnyi, V.A.; Fakhrutdinova, E.D.; Nazarova, T.S.; Kulinich, S.A.; Vodyankina, O.V. Comparative study of bismuth composites obtained via pulsed laser ablation in a liquid and in air for photocatalytic application. *Solid State Phenom.* **2020**, *312*, 172–178. [CrossRef]
48. Golubovskaya, A.G.; Fakhrutdinova, E.D.; Svetlichnyi, V.A. Bismuth silicates: Preparation by pulsed laser ablation and photocatalytic activity. *Proc. SPIE* **2021**, *12086*, 120861Y. [CrossRef]
49. Svetlichnyi, V.A.; Shabalina, A.V.; Lapin, I.N.; Goncharova, D.A.; Kharlamova, T.S.; Stadnichenko, A.I. Comparative Study of Magnetite Nanoparticles Obtained by Pulsed Laser Ablation in Water and Air. *Appl. Surf. Sci.* **2019**, *467–468*, 402–410. [CrossRef]
50. Yang, J.; Xie, T.; Liu, C.; Xu, L. Facile Fabrication of Dumbbell-like β-Bi_2O_3/Graphene Nanocomposites and Their Highly Efficient Photocatalytic Activity. *Materials* **2018**, *11*, 1359. [CrossRef]
51. Valencia, G.K.; Lopez, A.; Hernandez-Gordillo, A.; Zanella, R.; Rodil, S.E. Stabilized β-Bi_2O_3 nanoparticles from $(BiO)_4CO_3(OH)_2$ precursor and their photocatalytic properties under blue light. *Ceram. Int.* **2018**, *44*, 22329–22338. [CrossRef]
52. Steele, J.A.; Lewis, R.A. In situ micro-Raman studies of laser-induced bismuth oxidation reveals metastability of β-Bi_2O_3 microislands. *Opt. Mater. Express.* **2014**, *4*, 2133–2142. [CrossRef]
53. Isik, M.; Delice, S.; Gasanly, N.M.; Darvishov, N.H.; Bagiev, V.E. Temperature-dependent band gap characteristics of 20 single crystals. *J. Appl. Phys.* **2019**, *126*, 245703. [CrossRef]
54. Hou, D.; Hu, X.; Wen, Y.; Shan, B.; Hu, P.; Xiong, X.; Qiao, Y.; Huanga, Y. Electrospun sillenite $Bi_{12}MO_{20}$ (M = Ti, Ge, Si) nanofibers: General synthesis, band structure, and photocatalytic activity. *Phys. Chem. Chem. Phys.* **2013**, *15*, 20698. [CrossRef]
55. Dou, L.; Jin, X.; Chen, J.; Zhong, J.; Li, J.; Zeng, Y.; Duan, R. One-pot solvothermal fabrication of S-scheme OVs-Bi_2O_3/Bi_2SiO_5 microsphere heterojunctions with enhanced photocatalytic performance toward decontamination of organic pollutants. *Appl. Surf. Sci.* **2020**, *527*, 146775. [CrossRef]
56. Isari, A.A.; Payan, A.; Fattahi, M.; Jorfi, S.; Kakavandi, B. Photocatalytic degradation of rhodamine B and real textile wastewater using Fe-doped TiO_2 anchored on reduced graphene oxide (Fe-TiO_2/rGO): Characterization and feasibility, mechanism and pathway studies. *Appl. Surf. Sci.* **2018**, *462*, 549–564. [CrossRef]
57. Hu, X.; Mohamood, T.; Ma, W.; Chen, C.; Zhao, J. Oxidative decomposition of Rhodamine B dye in the presence of VO_2^+ and/or Pt(IV) under visible light irradiation: N-deethylation, chromophore cleavage, and mineralization. *J. Phys. Chem. B* **2006**, *110*, 26012–26018. [CrossRef]
58. Fernández-Castro, P.; Vallejo, M.; San Román, M.F.; Ortiz, I. Insight on the fundamentals of advanced oxidation processes. Role and review of the determination methods of reactive oxygen species. *J. Chem. Technol. Biotechnol.* **2015**, *90*, 796–820. [CrossRef]
59. Li, J.; Xu, Y.; Zhang, M.; Wang, D. Determination of Furfural and 5-Hydroxymethylfurfural in Biomass Hydrolysate by High-Performance Liquid Chromatography. *Energy Fuels* **2017**, *31*, 13769–13774. [CrossRef]
60. Franca, J.R.; Souza, P.B.; Dias, J.G.; Perdomo, A.D.P.; Linhares, A.A.; Bassoli, W.R.B.; Schafer, D.; Pasa, A.A.; Cid, C.C.P. Photocurrent in Bi_2Se_3 films electrodeposited with predominance of the orthorhombic phase. *Electrochim. Acta* **2023**, *463*, 142791. [CrossRef]
61. Attard, A.E. Theory of origins of the photorefractive and photoconductive effects in $Bi_{12}SiO_{20}$. *J. Appl. Phys.* **1991**, *69*, 44–55. [CrossRef]
62. Frejlich, J. *Photorefractive Materials: Fundamental Concepts, Holographic Recording and Materials Characterization*; John Wiley & Sons, Inc.: Hoboken, NJ, USA, 2007; pp. 19–43, ISBN 978-0-471-74866-3.
63. Murashkina, A.A.; Bakiev, T.V.; Artemev, Y.M.; Rudakova, A.V.; Emeline, A.V.; Bahnemann, D.W. Photoelectrochemical behavior of the ternary heterostructured systems CdS/WO_3/TiO_2. *Catalysts* **2019**, *9*, 999. [CrossRef]